

Bimodal atomic force microscopy for the characterization of thiolated self-assembled monolayers

SUPPORTING INFORMATION

SELECTION OF CONTACT MECHANICS MODEL

Under the operating conditions, the tip interacts with short range repulsive forces, allowing information on the mechanical properties of the sample to be accessed.¹ An elastic contact between the tip and sample is assumed. Conservative forces are considered dominant and non-conservative forces, such as viscoelasticity² and adhesion hysteresis, negligible. Experimentally, the above-mentioned assumptions were confirmed by performing a series of force-distance curves on the alkanethiol SAMs used. No SAM showed a viscoelastic response. Moreover, adhesion hysteresis was less than 10% of the applied force for all SAMs, and almost non-existent for freshly prepared samples.

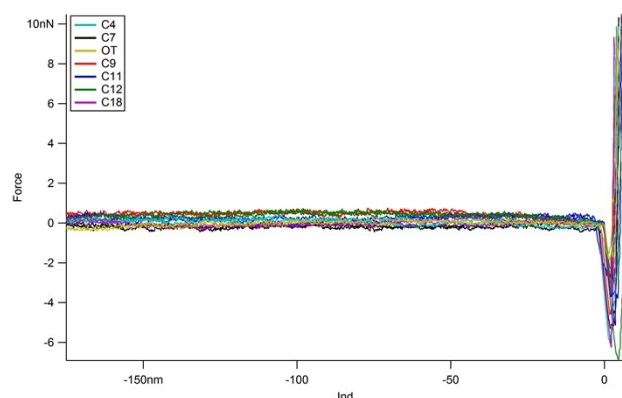


Figure SI.1: Force-indentation curves for all tested alkanethiol SAMs. No viscoelastic component can be observed.

The tip-sample interaction is modeled using the Hertz contact model. Under the operating conditions no plastic deformation of the monolayers is observed, supporting the assumption of an elastic contact. In the recorded force-distance curves an adhesive component was observed. Using the adhesion map proposed by Johnson and Greenwood³ and the information on W_{adh} as extracted from the force curves, the elastic contact between the tip and sample can be modeled using the Hertz contact model. Contact models such as the Derjaguin-Mueller-Toporov (DMT) model do take into account adhesive forces outside the area of contact. The selection of the contact mechanics model was further confirmed by calculating the effective surface Young's moduli, E^* , of the used alkanethiol SAMs via force spectroscopy, and fitting the data with both Hertz and DMT model. The difference between the two values did not exceed 11.7% (maximum difference calculated, for freshly prepared C8 SAM), while for most SAMs it was found less than 5%. In every case, the difference of E^* between the two models was smaller than the standard deviation of the values within each model. We therefore conclude that the use of the Hertz model to describe the interaction between the tip and sample is a fair approximation and does not introduce a significant error in the calculated values.

Table SI.1: Comparison of E^* for alkanethiol SAMs as determined via force-distance curves and calculated using the Hertz model (E_{Hertz}^*) and the DMT model (E_{DMT}^*).

Sample	$E_{Hertz} \pm \sigma$ (GPa)	$E_{DMT} \pm \sigma$ (GPa)	$(E_{Hertz} - E_{DMT}) \%$
C4	1.512 \pm 0.592	1.497 \pm 0.391	1.00%
C7	1.742 \pm 0.670	1.818 \pm 0.657	-4.27%
C8	1.919 \pm 0.617	1.935 \pm 0.586	-0.83%
C9	1.739 \pm 0.622	1.746 \pm 0.874	-0.40%
C11	1.304 \pm 0.294	1.347 \pm 0.249	-3.24%
C12	1.686 \pm 1.112	1.737 \pm 0.656	-2.98%
C18	2.178 \pm 0.753	1.937 \pm 0.639	11.71%

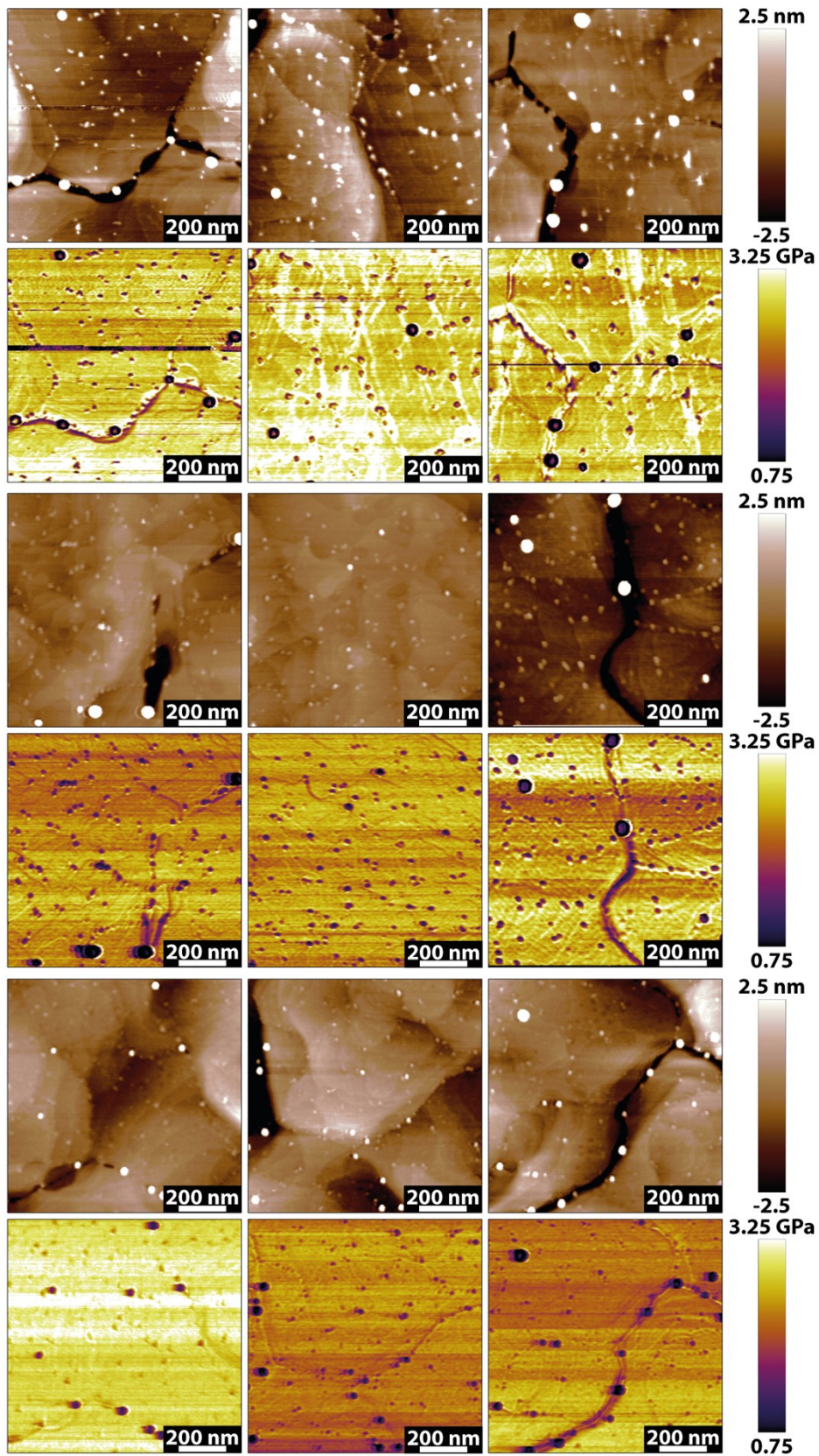


Figure SI.2: Representative topography and corresponding E^* for three samples of C4 SAMs. Each row corresponds to one sample. The white dots correspond to ambient contamination and appear during scanning. Their occurrence can be minimized by thoroughly drying the samples under vacuum prior to scanning and minimization of sample exposure to ambient conditions.

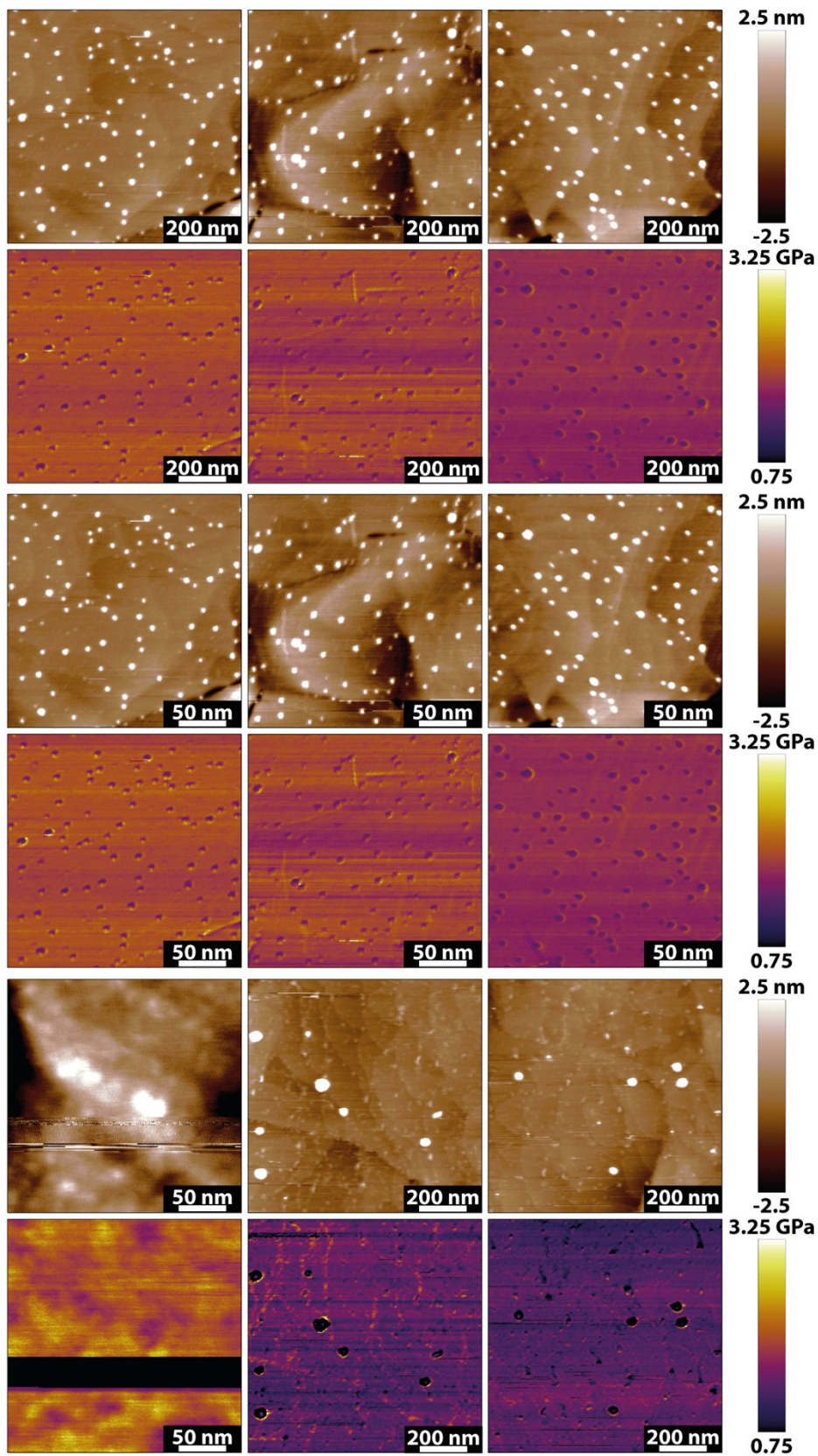


Figure SI.3: Representative topography and corresponding E^* for three samples of C7 SAMs. Each row corresponds to one sample. The white dots correspond to ambient contamination and appear during scanning. Their occurrence can be minimized by thoroughly drying the samples under vacuum prior to scanning and minimization of sample exposure to ambient conditions.

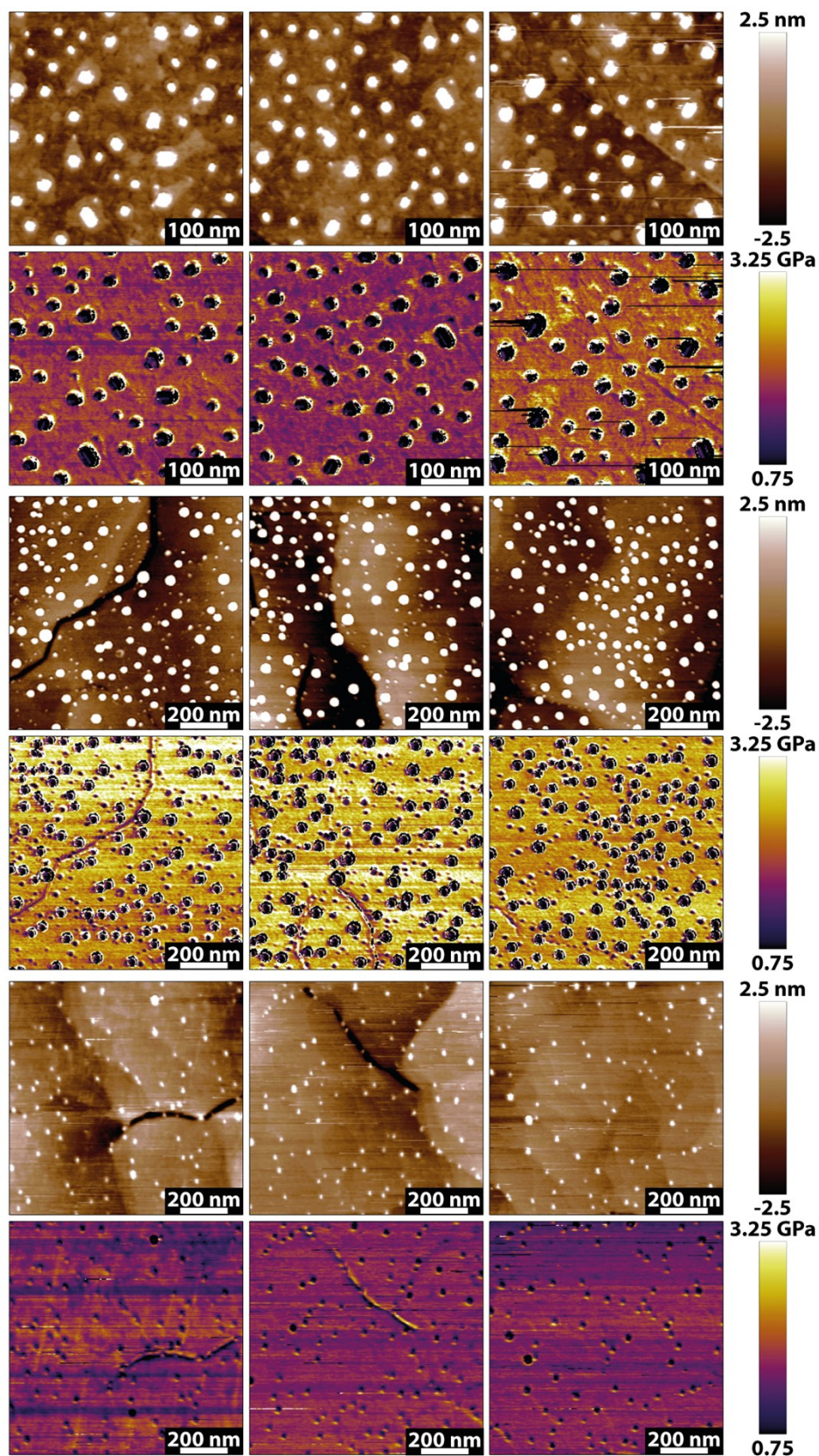


Figure SI.4: Representative topography and corresponding E^* for three samples of C8 SAMs. Each row corresponds to one sample. The white dots, present mostly in the first sample, correspond to ambient contamination and appear during scanning. Their occurrence can be minimized by thoroughly drying the samples under vacuum prior to scanning and minimization of sample exposure to ambient conditions.

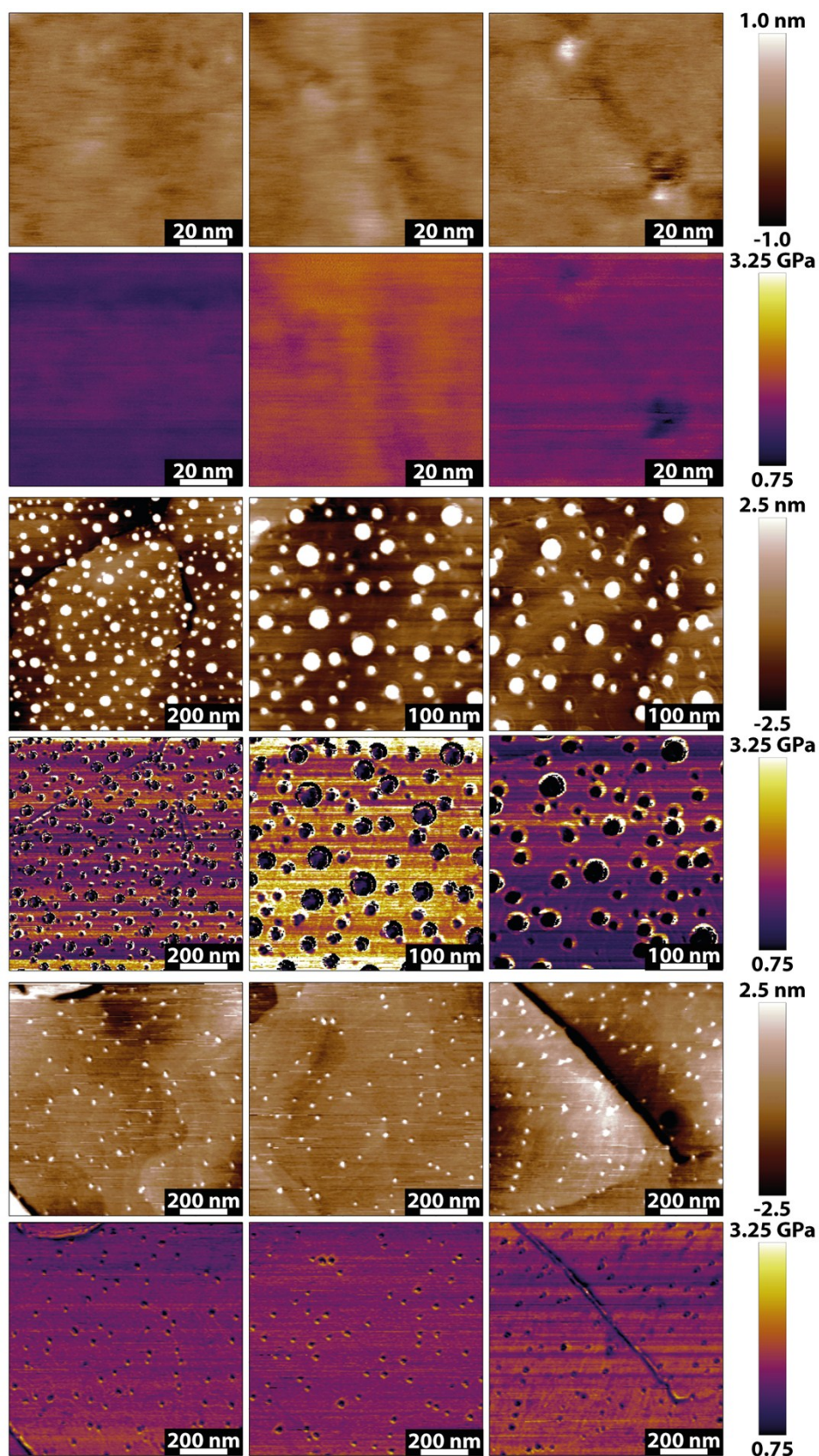


Figure SI.5: Representative topography and corresponding E^* for three samples of C9 SAMs. Each row corresponds to one sample. The white dots, present mostly in the second sample, correspond to ambient contamination and appear during scanning. Their occurrence can be minimized by thoroughly drying the samples under vacuum prior to scanning and minimization of sample exposure to ambient conditions.

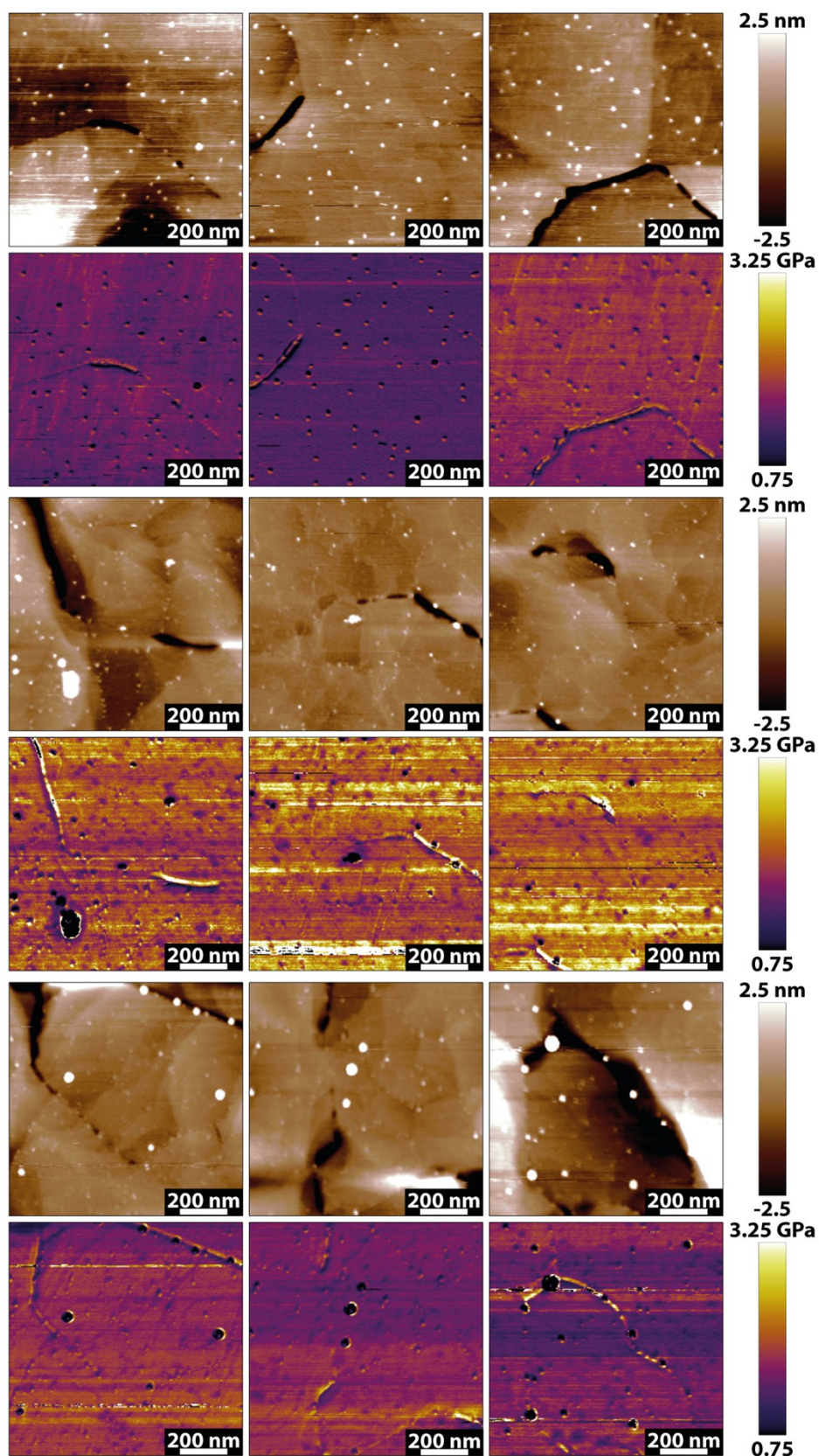


Figure SI.6: Representative topography and corresponding E^* for three samples of C11 SAMs. Each row corresponds to one sample. The white dots, present mostly in the first sample, correspond to ambient contamination and appear during scanning. Their occurrence can be minimized by thoroughly drying the samples under vacuum prior to scanning and minimization of sample exposure to ambient conditions.

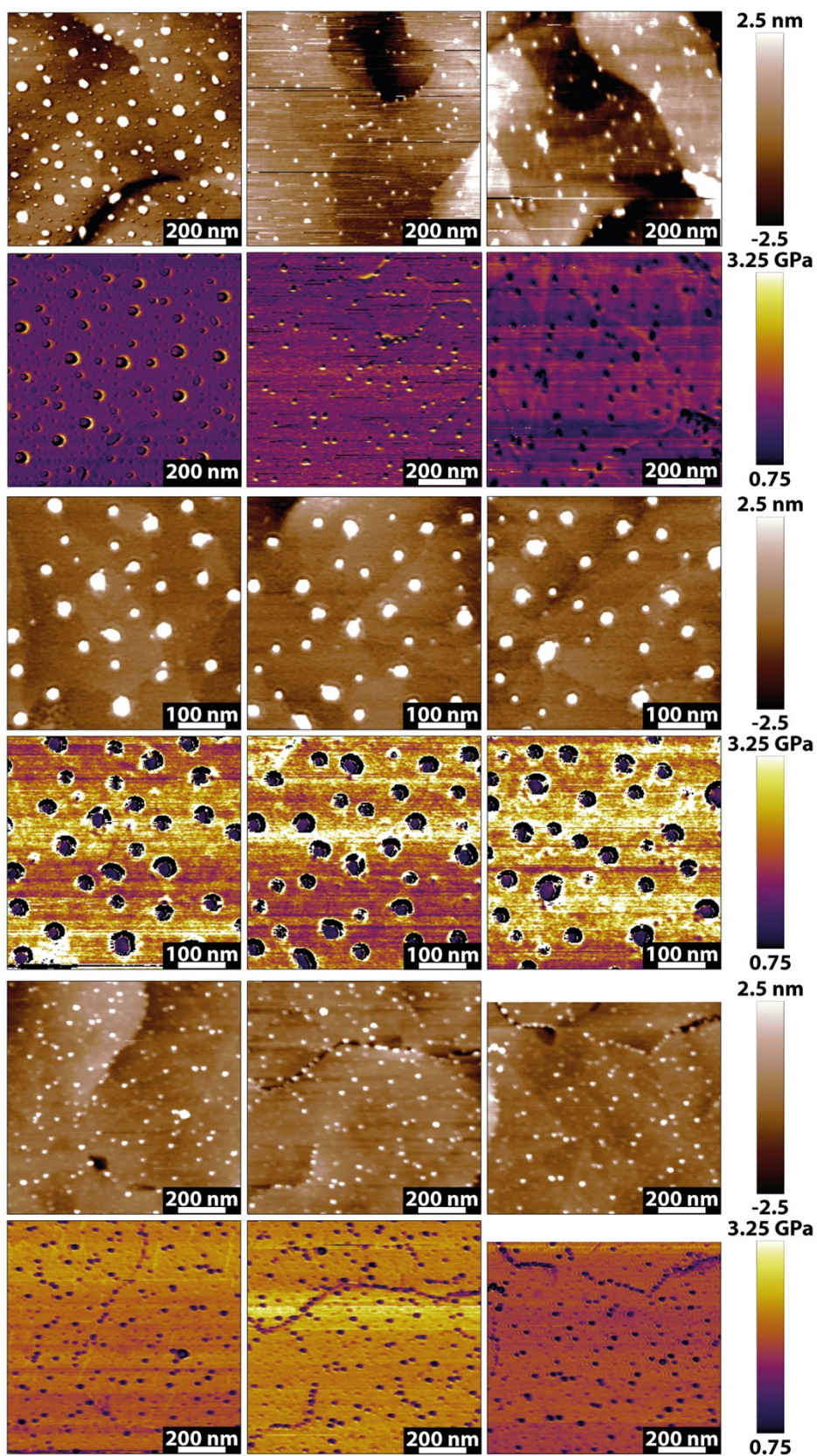


Figure SI.7: Representative topography and corresponding E^* for three samples of C12 SAMs. Each row corresponds to one sample. The white dots, present mostly in the first and second sample, correspond to ambient contamination and appear during scanning. Their occurrence can be minimized by thoroughly drying the samples under vacuum for a week prior to scanning and minimization of sample exposure to ambient conditions.

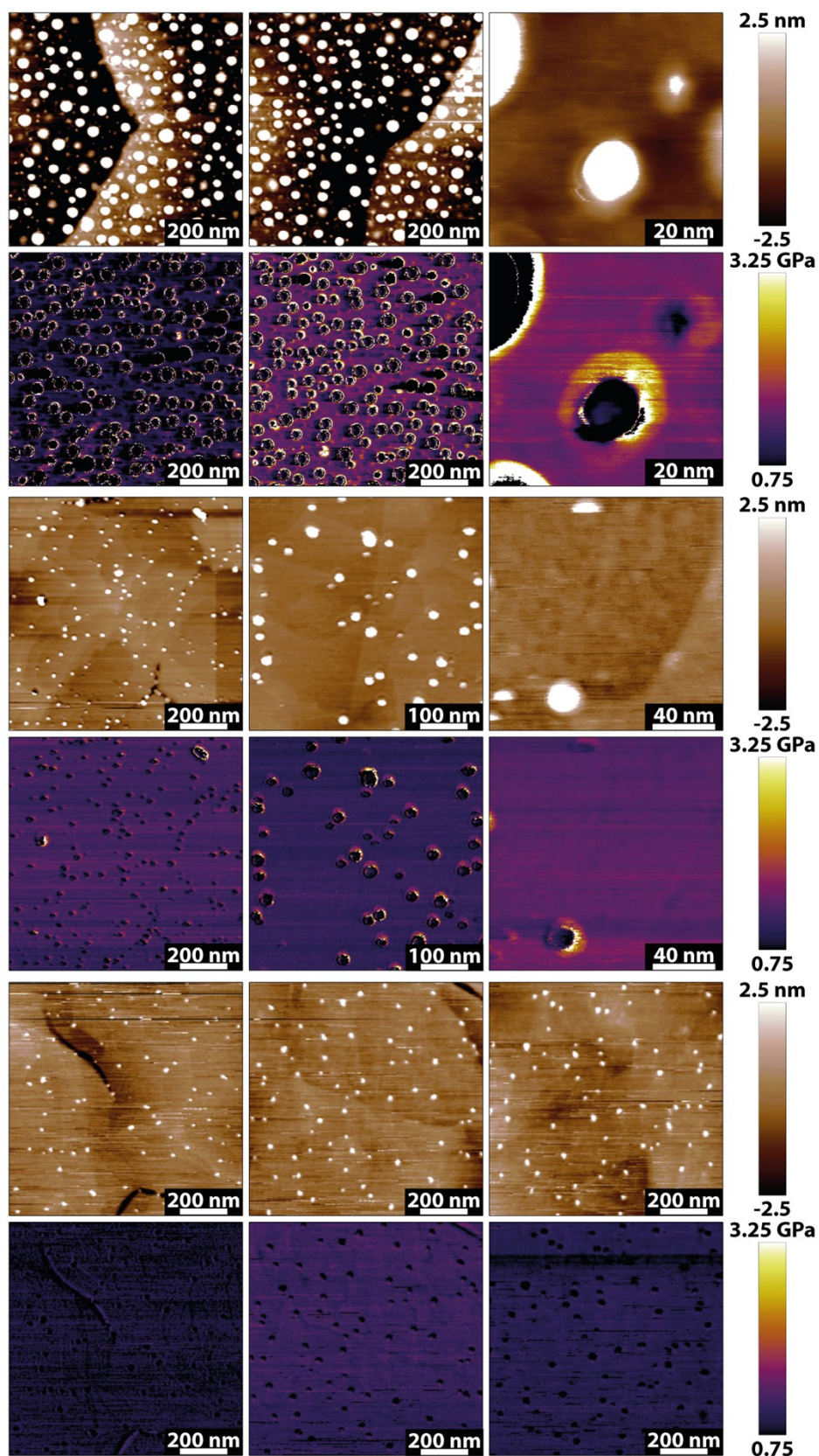


Figure SI.8: Representative topography and corresponding E^* for three samples of C18 SAMs. Each row corresponds to one sample. The white dots, present mostly in the first sample, correspond to ambient contamination and appear during scanning. Their occurrence can be minimized by thoroughly drying the samples under vacuum for a week prior to scanning and minimization of sample exposure to ambient conditions.

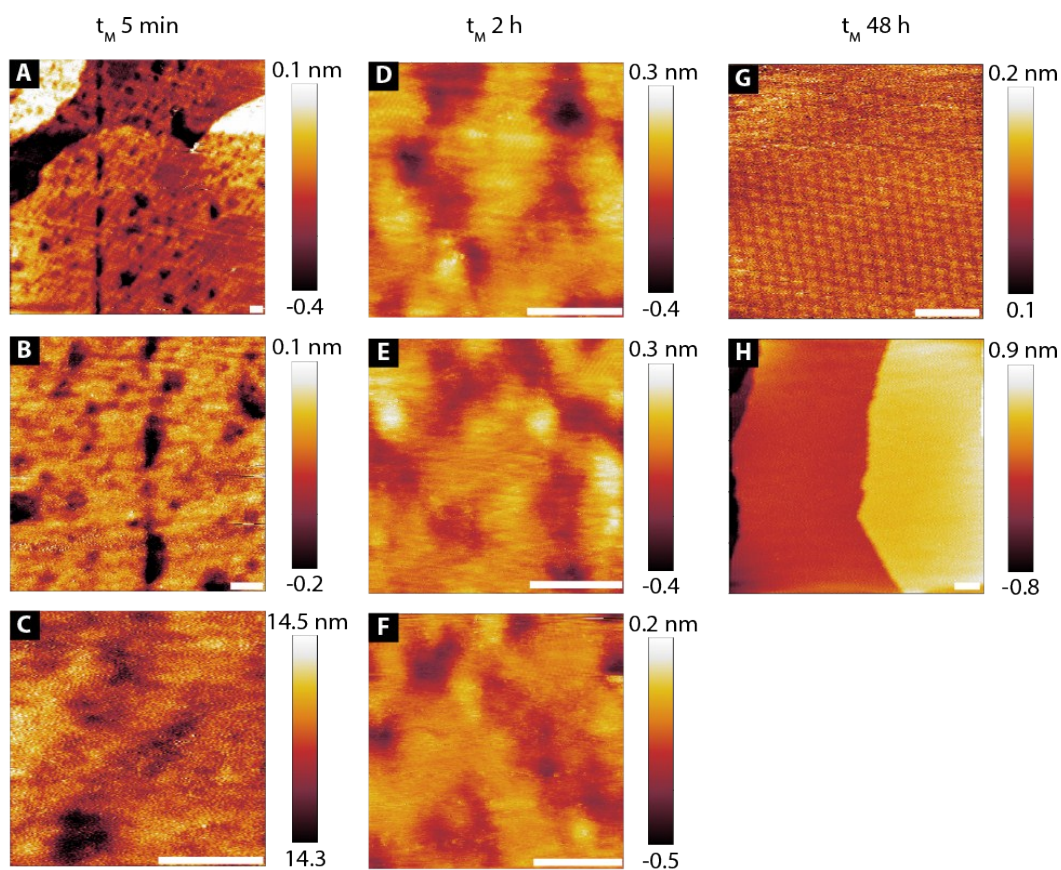


Figure SI.9 (A-I): Representative images of C8 SAMs' topography at different t_M , as recorded by STM. At $t_M = 5$ min only a submonolayer has been formed. At $t_M = 2$ h a crystalline stand-up phase, evident as dots on a grid with 0.4 nm period, coexists with an amorphous phase. At $t_M = 48$ h the surface is covered by a well-ordered, stand-up crystalline phase. Scale bar 10 nm (A-F, H), 2 nm (G).

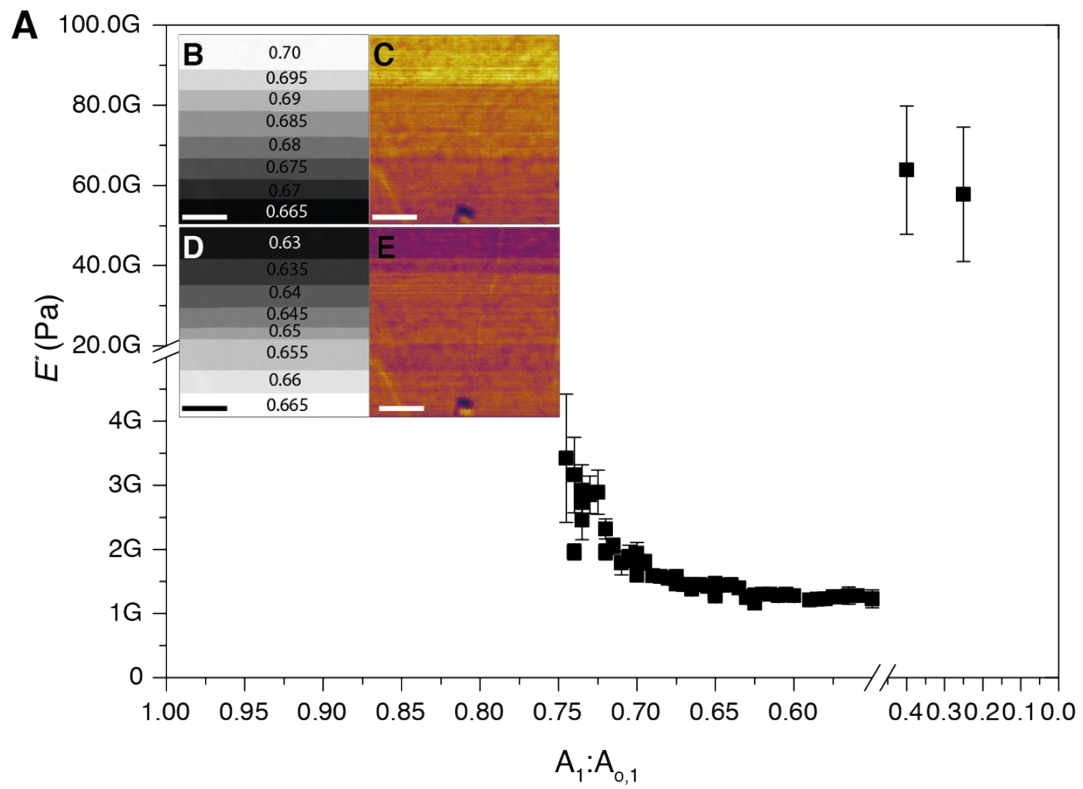


Figure SI.10: E^* dependence on imaging conditions experimentally determined at 400kHz for octanethiol SAMs (A). Work (A_1) to free ($A_{0,1}$) amplitude ratio (B, D) and corresponding E^* (C, E respectively). Scale bar 100 nm.

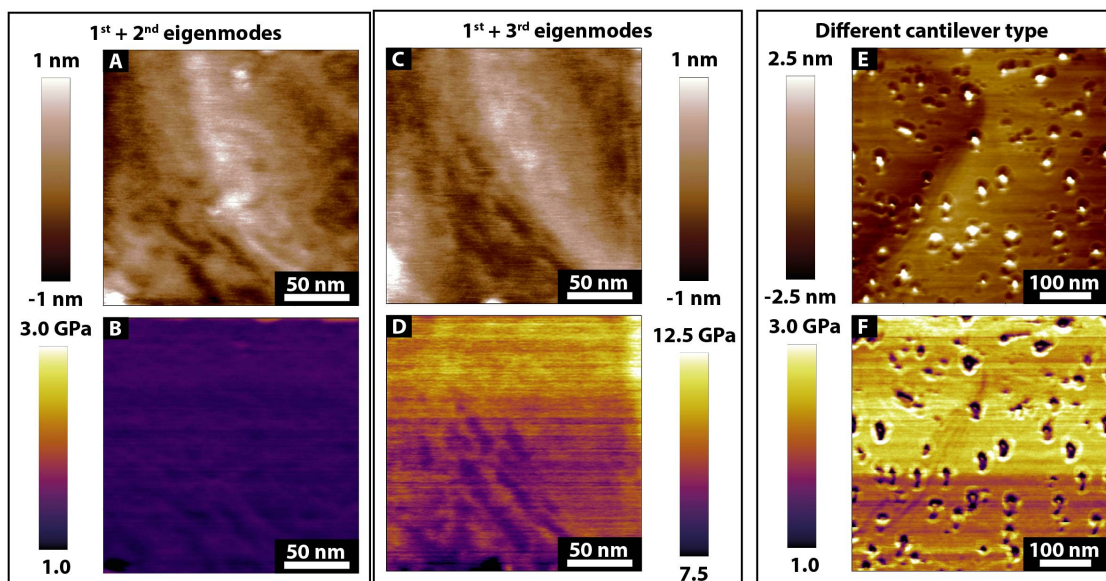


Figure SI.11 (A-F): Topography and E^* of C8 SAMs recorded via bimodal AFM using calibrated cantilevers. The same area of the sample was consecutively scanned using different combination of eigenmodes for the same calibrated cantilever: 1st and 2nd (A, B) and 1st and 3rd (C, D). Using a different higher eigenmode and probing the sample at a different frequency leads to numerically different values of E^* . Using a different cantilever type (AC200TS, $k_1 = 10$ nN/nm, $f_{o,1} = 150$ kHz) also leads to calculation of different numerical values of E^* , even though the overall trend remains the same. Deconvolution of the effect of the substrate eliminates this effect, however if the purpose of the measurement is a direct comparison between molecularly thin films, consistent use of the same cantilever type and eigenmode combination is important.

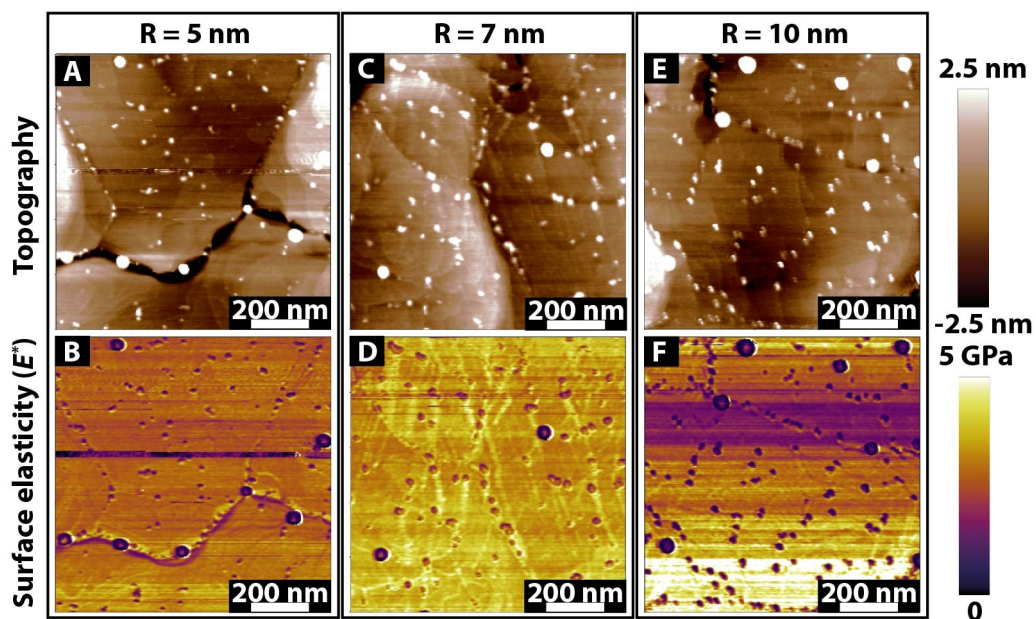


Figure SI.12 (A-F): Recorded topography and E^* images of a C4 SAM at the 1st (A, B), 4th (C, D) and 15th (E, F) scan of the surface. Between the scans the cantilever tip radius, R , was recalibrated and found to vary significantly, as a result of tip contamination. For the first scan R was found equal to 5 nm, value which increased to 7 nm after 5 scans. After 15 scans R was equal to 10 nm. The displayed E^* images have all been calculated based on a nominal tip radius $R = 5$ nm, in order to show the possible large variations in experimentally determined E^* of SAMs, if the cantilever tip is not rigorously monitored for contamination and frequently recalibrated.

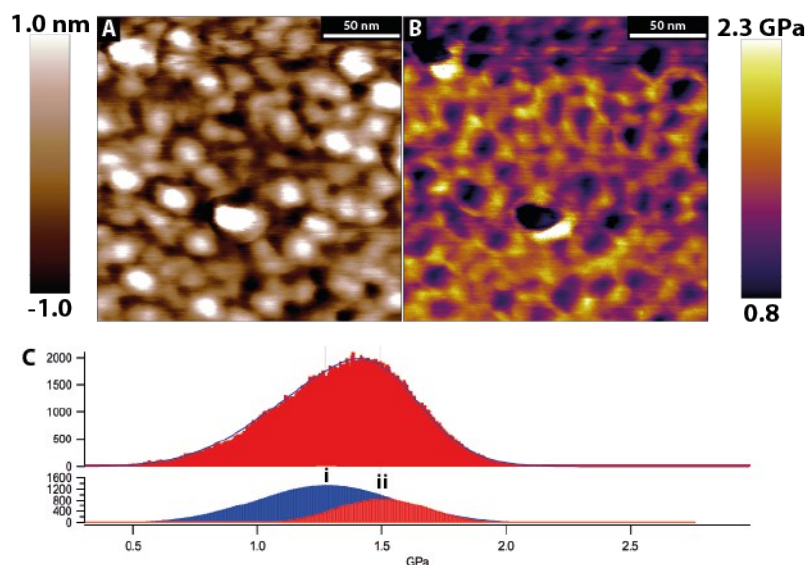


Figure SI.13: Topography (A) and surface elasticity (B) of homoligand trimethylaminedecanethiol (TMA) SAMs as recorded via bimodal AFM. TMA has a bulky, charged headgroup, which, on the one hand discourages the close packing of ligands, and on the other hand facilitates the formation of bilayer islands on top of an already formed underlying SAM. The topography channel shows that TMA SAMs appear to be composed of taller and shorter areas. The height difference between the two corresponds to the length of a fully extended TMA molecule, 1.7nm, supporting the hypothesis of bilayer island formation on top of one fully formed SAM. The tall and short areas, conversely the bilayer islands and underlying monolayer, show differences in the measured values of E^* . Deconvoluting the distribution of E^* for a TMA SAM allows the fitting of the peak by two separate gaussians, further underlying the coexistence of two distinct phases: a stiffer, shorter, monolayer, and softer, taller bilayer islands. The average E^* of the synthesized SAMs was measured at $1.32 \text{ GPa} \pm 0.18 \text{ GPa}$, much softer than E^* of C9 or C11 SAMs, as the bulky headgroup discourages the close packing of ligands.

References:

- (1) Proksch, R. Multifrequency, Repulsive-Mode Amplitude-Modulated Atomic Force Microscopy. *Appl. Phys. Lett.* **2006**, *89* (11), 1–4.
- (2) Herruzo, E. T.; Perrino, A. P.; Garcia, R. Fast Nanomechanical Spectroscopy of Soft Matter. *Nat. Commun.* **2014**, *5*, 3126.
- (3) Johnson, K. L.; Greenwood, J. A. An Adhesion Map for the Contact of Elastic Spheres. *J. Colloid Interface Sci.* 1997, pp 326–333.